

Title

**Particle deposition on the saturnian satellites from ephemeral cryovolcanism on Enceladus**

Authors

**Naoyuki Hirata <sup>a</sup>, Hideaki Miyamoto <sup>a, b, \*</sup>, and Adam P. Showman <sup>c</sup>**

Authors' affiliation

**a The University Museum, The University of Tokyo, Hongo, Tokyo 113-0033, Japan.**

**b Planetary Science Institute, 1700E Ft. Lowell, Suite 106, Tucson, AZ 85719, USA**

**c Department of Planetary Sciences, Lunar and Planetary Laboratory, University of Arizona, Tucson, AZ 85721, USA**

**\* Corresponding author E-mail address: [hm@um.u-tokyo.ac.jp](mailto:hm@um.u-tokyo.ac.jp)**

## **Abstract**

The geologically active south pole of Enceladus generates a plume of micron-sized particles, which likely form Saturn's tenuous E-ring extending from the orbit of Mimas to Titan. Interactions between these particles and satellites have been suggested, though only as very thin surficial phenomena. We scrutinize high-resolution images with a newly developed numerical shape model of Helene and find that the leading hemisphere of Helene is covered by thick deposits of E-ring particles, which occasionally collapse to form gully-like depressions. The depths of the resultant gullies and near-absence of small craters on the leading hemisphere indicate that the deposit is tens to hundreds of meters thick. The ages of the deposits are less than several tens of My, which coincides well with similar deposits found on Telesto and Calypso. Our findings as well as previous theoretical work collectively indicate that the cryovolcanic activity currently occurring on Enceladus is ephemeral.

## **1 Introduction**

Mid-sized satellites in the E-ring system, such as Tethys and Dione (co-orbital moon of Helene), show almost bimodal distributions of albedo [Buratti et al., 1990; Verbiscer and Veverka, 1992] and visual and infrared spectra [Pitman et al., 2010]. For example, the leading hemisphere of Dione at visible wavelengths is 1.8 times brighter than the trailing hemisphere [Jaumann et al., 2009], which has been suggested to result from differential accumulation of E-ring material on its surface [Ostro et al., 2010; Verbiscer et al., 2007] and/or by bombardment of corotational plasma and energetic electrons [Schenk et al., 2011]. However, no depositional features have been reported on satellites in the E-ring region except for those on Enceladus (e.g., buried craters) [Kirchoff and Schenk, 2009]. We thoroughly examine all high-resolution images obtained by the Cassini spacecraft through November 2013 and find that possible depositional features ubiquitously exist on small satellites in the E-ring region. The best examples are found on Helene because it is the most extensively imaged small satellite in the E-ring.

## **2 Geological Study of Helene**

Like most saturnian satellites, Helene has numerous craters. Using high-resolution images, we identify more than 70 craters (see Crater on Helene in supporting information). Interestingly, Helene shows a bimodal appearance—the heavily cratered trailing hemisphere exhibits a crater density ten times greater than the smooth-looking leading hemisphere (Figure 1). In the case of Enceladus, the deficiency of craters has

been suggested to result from a combination of viscous relaxation and burial of craters by both the south polar plume and possibly E-ring material [Kirchoff and Schenk, 2009]. However, a small satellite, such as Helene, is not disturbed by endogenic activity, which provides an optimal situation to examine its possible interactions with E-ring materials.

We study 437 high-resolution images of Helene (500 m/pixel or better) obtained by the Cassini spacecraft through 7 flybys between 2006 and 2011 and find that Helene has numerous, sharply curved gully-like depressions (hereafter streaky depressions; Figure 2). Streaky depressions exist on slopes on the leading hemisphere typically as a group exhibiting similar orientations. These streaky depressions on the leading hemisphere can be identified on images whose resolutions are as high as 200 m/pixel; however, images of the trailing hemisphere, whose resolutions are better than 200 m/pixel, do not show similar features. This indicates that no streaky depressions exist on the trailing hemisphere (Figure 2d).

We construct a numerical shape model of Helene to calculate the local gravitational gradients (Figure 1; see Numerical shape model in supporting information) and critically compare these gradients to the distribution of streaky features (Figure 3). We find that streaky depressions exist only on slopes and strictly follow the local gravitational slopes (Figure 3), which indicates that the streaky depressions result from gravity-induced mass movements. Terrestrial gullies sometimes show structures—such as alcoves (funnelform depressions extending from the top of the slope), channels (linear depressions extending from the narrow stem of an alcove), and fans (cone-shaped deposits crossed by streams)—that indicate transport of material from the top to bottom of the slopes [McClung and Schaerer, 1993]. Analogously to such terrestrial gullies, streaky depressions on Helene sometimes exhibit alcoves and channels (Figures 2b and 2c), further supporting the idea that streaky depressions are formed by gravity-induced mass movements.

The slope angles where streaky depressions exist generally range from  $7 \pm 3$  degrees to 20 degrees, which is significantly smaller than the friction angles of terrestrial rock materials (typically, 25–30 degrees or larger [Lambe and Whitman, 1979]). This observation indicates that streaky depressions form in material which collapses easily and exhibits a small friction coefficient, such as fine particulate material rather than massive ice blocks. Perhaps, such fine particles continuously collapse and form the streaky depressions. We conclude that the leading hemisphere of Helene is generally covered by such fine particles because (i) the leading hemisphere generally appears smooth as evidenced by the lack of shadows, even in areas with large illumination angles; (ii) almost no small craters can be identified on the leading

hemisphere; and (iii) large craters exhibit flattened shapes. Together, these lines of evidence indicate that deposition of fine particles has modified or erased craters on the leading hemisphere.

### **3 Discussion**

#### **3.1 Plumes From Enceladus Feed Small Satellites**

Spectral analysis [Filacchione et al., 2013] shows that the color of Helene is similar to that of Enceladus. Also, in orbits far beyond Enceladus, satellites are expected to overtake E-ring particles (i.e., Enceladus-derived particles), which would result in preferential deposition on the leading hemisphere of Helene. Moreover, E-ring particles are known to be fine particles [Kargel, 2006], consistent with the apparent fine particulate nature of deposits on Helene's leading hemisphere. These facts indicate that the deposit on Helene comes from the E-ring.

Our findings indicate that ice particles ejected from Enceladus are preferentially deposited on Helene's leading hemisphere, and that the resulting deposits occasionally collapse to form streaky depressions. Motivated by this finding, we identified similar deposits on other small satellites in the E-ring region, such as Telesto and Calypso (Tethys' Trojan satellites), Pallene, and Methone (Figure 2 and S1 in supporting information), where higher brightness (i.e., presumably higher densities) of the ring is reported [Verbiscer et al., 2007]. For example, craters on Telesto and Calypso generally exhibit softened, blanketed morphologies with indistinct rims (and sometimes such craters are almost entirely erased), similar to craters on the leading hemisphere of Helene. In fact, even large (>5 km diameter) craters on Telesto and Calypso appear to be buried just as small craters are on Helene. Also, Calypso exhibits streaky depressions (Figure 2e), which are similar to those on Helene. Spectral observations demonstrate the contribution of E-ring material on their surfaces [Buratti et al., 2010], which supports the view that, as with Helene, E-ring material accumulated on these satellites into thick deposits. Moreover, high-resolution images of Pallene (Figure 2g), one of the three Alkyonides satellites, indicate a circular outline with a sharp terminator line lacking any undulations even at the highest resolution of about 500 m/pixel. This implies that Pallene has a featureless spherical shape, which is unusual for a body of only ~2.2 km radius. Methone (Figure 2h), one of the other two Alkyonides satellites, is likely quite similar to Pallene in terms of size, shape, and smooth appearance [e.g., Thomas et al., 2013]. The shapes of these bodies are also possibly related to the accumulation of E-ring material on their surfaces, as such material can cover the original irregular topography.

### **3.2 Lack of Hemispheric Dichotomy for Telesto/Calypso**

Unlike Helene, Telesto and Calypso appear to have smooth surfaces and few small craters even on their trailing hemispheres (though Calypso's trailing hemisphere has yet to be observed at high resolution), which suggests that Telesto and Calypso lack any dichotomy (see Figure S1 in supporting information). This diversity may be explained by the motion of the E-ring particles.

The mean velocity difference of a particle ejected from Enceladus relative to an encountered satellite will depend on distance from Saturn. This would naturally cause the impact distribution of particles onto the satellite surface to vary with distance from Saturn as well (see Lack of hemispheric dichotomy for Telesto/Calypso in supporting information). (i) Inside the orbit of Enceladus, particles generally move faster than encountered satellites, which results in deposition on the trailing hemisphere, as is observed for Mimas. (ii) In the orbit immediately beyond Enceladus, the mean relative velocity is modest but non-zero. Particles will move both faster and slower than encountered moons, but on average will be slightly slower. This can explain the small but not negligible albedo difference (1.1 times) between the leading and trailing hemisphere of Tethys (a co-orbital moon of Telesto and Calypso). Still, particles will encounter both the leading and trailing hemisphere of encountered satellites, and this can explain the deposition everywhere on Telesto and Calypso. (iii) Finally, in orbits far beyond Enceladus, the mean relative velocities may be large, with satellites rapidly overtaking Enceladus-derived particles, which results in preferential deposition on the leading hemisphere of Helene, Dione, and Rhea. We note that bombardment by corotational plasma or energetic electrons also influences the color and albedo pattern on mid-sized E-ring satellites [Schenk et al., 2011].

The lack of a hemispheric dichotomy on Telesto and Calypso may be due to not only E-ring particle dynamics but also to possible non-synchronous rotation of these satellites. Non-synchronous rotation re-orientates the satellite, causing the leading and trailing hemispheres to migrate across the satellite figure and preventing preferential particle deposition on any specific hemisphere of the satellite. In addition to Telesto and Calypso, Pallene and Methone also appear to lack any hemispheric dichotomy. This may likewise be explained by E-ring particle dynamics or non-synchronous rotation; however, the depositional mechanics on Pallene or Methone may be more complex (see Deposition of ring particles on Pallene and Methone in supporting information).

### **3.3 Thickness of E-Ring Deposits**

Shadows of streaky depressions indicate that their depths are typically a few tens of meters, which implies that the particle deposits in which the depressions form

must be at least tens of meters thick. Moreover, the leading hemisphere shows the near-absence of small craters (less than  $\sim 3$  km across; Figure 1c). This indicates that the deposits are unlikely to be more than a few hundred meters thick. Therefore, we estimate that the thickness of the deposits on Helene accumulated from the E-ring is between 10 and 300 m.

On the other hand, Telesto and Calypso almost completely lack large ( $>5$  km diameter) craters. Moreover, the few existing craters are almost entirely erased. This fact suggests that E-ring deposits on Telesto and Calypso are roughly twice as deep as those on Helene. This difference may be due to the densities of E-ring. The E-ring is known to be denser closer to Enceladus [Verbiscer et al., 2007]. Therefore, the E-ring at the orbit of Telesto/Calypso exhibits higher brightness than at the orbit of Helene, which may explain the thicker deposits on Telesto/Calypso relative to those on Helene.

Unlike the deposits on these small satellites, the E-ring deposits on Tethys and Dione are probably quite thin because (1) these satellites' radar-optical albedo appears to decrease with distance from Enceladus [Ostro et al., 2010]; (2) crater statistics [Kirchoff and Schenk, 2010] indicate no deficiency of craters on either Tethys or Dione, in contrast to Helene and Telesto; and (3) high-resolution images of Tethys and Dione show no unambiguous evidence for thick deposits, such as streaky depressions. Nevertheless, albedo [Verbiscer et al., 2007], spectral [Filacchione et al., 2010], and thermal inertia [Howett et al., 2010] measurements indicate thin but non-zero deposits of E-ring particles on these mid-size satellites. Thus, the E-ring particles are likely deposited widely on Tethys and Dione, but the resulting deposits are much thinner than those on the small satellites. The reasons for this difference are unknown. Possible explanations are differences in the dynamics of E-ring particles among the satellites or higher impact velocity onto the mid-sized satellites.

#### **4 Implication for Ephemeral Cryovolcanism on Enceladus**

We perform an age estimate of the E-ring deposits based on the cratering rate. The high crater density on the trailing hemisphere of Helene indicates that Helene is basically an old object. Based on the crater chronology of the saturnian system [Zahnle et al., 2003], we estimate that the surface age of the heavily cratered terrain on the trailing hemisphere is  $\sim 4.0$  Gy (and at least  $\sim 1.0$  Gy), which coincides with the age estimated from the distribution of large ( $>5$  km) craters (Figure 1c). We also find that the distributions of craters exceeding 5 km in diameter on Helene and Telesto are generally similar to those of Dione and Tethys [Kirchoff and Schenk, 2010] (Figure 1c), which indicates that, in general, the original crater densities of small satellites are similar for

these mid-sized satellites. Thus, Helene, Telesto, and Calypso probably have similar formational ages, which are significantly older than that of the E-ring deposits.

On Helene's E-ring deposit, whose area is 1637 km<sup>2</sup> estimated from our shape model, we identify five craters of ~200 m diameter but no craters exceeding 1 km in diameter. If we adopt standard cratering-rate estimates for the outer solar system [Zahnle et al., 2003], the best estimates for deposit ages are several tens of My or younger (see Age estimates based on cratering rate in supporting information). The crater size-frequency distribution of the trailing hemisphere of Telesto is similar to that of the leading hemisphere of Helene.

Interestingly, several lines of evidence suggest that Enceladus has not been active at its current level over solar-system history. For example, Kargel [2006] shows that no geological evidence exists to support a large change in its radius, which would be expected if the current mass-loss rates have been maintained through Enceladus' lifetime. Moreover, Roberts and Nimmo [2008] show that the current energy output of Enceladus is difficult to sustain over solar-system history. Enceladus' current heat flux greatly exceeds that occurring in equilibrium with its current eccentricity given the time-averaged  $Q$  of Saturn [Meyer and Wisdom, 2007], suggesting that the current activity may be greater than average. Recent global geophysical models show that Enceladus can exhibit episodic activity, with short periods of intense activity interspersed with long quiescent epochs [Showman et al., 2013]. These studies are consistent with our views. Thus, there is the possibility that the accumulation of E-ring material on small satellites in this region began several My ago as a result of the initiation of cryovolcanism of Enceladus.

### **Acknowledgments**

This work is supported in part by Grant-in-Aid for JSPS Fellows (to NH), JSPS KAKENHI (to HM), and the NASA Origins program (to APS). We use the raw data freely available via NASA's Planetary Data System (<http://pds.nasa.gov/>).

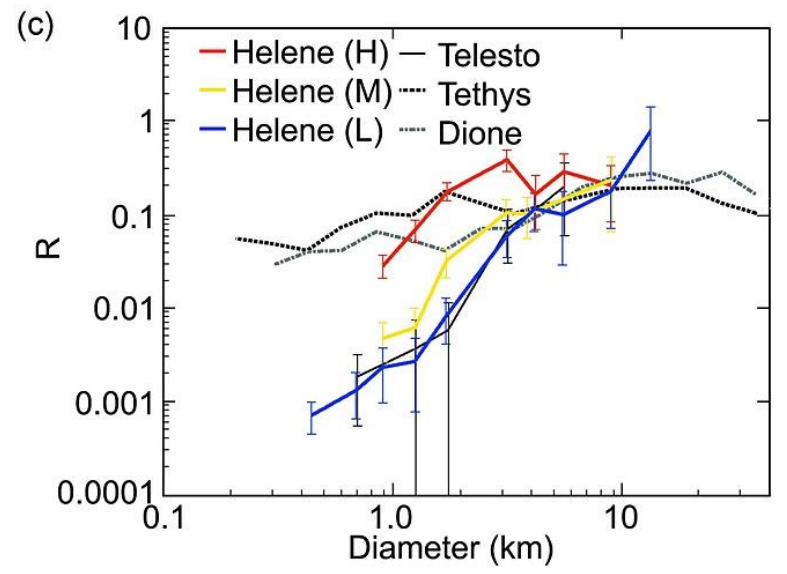
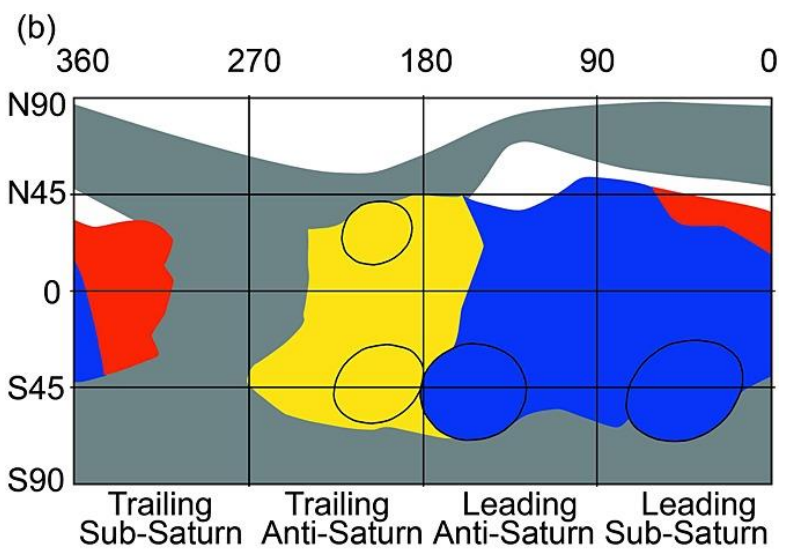
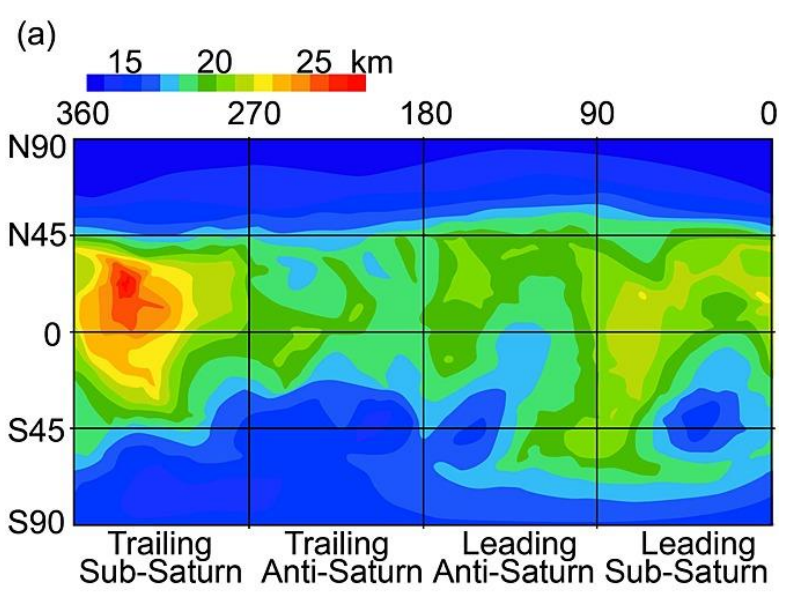




**Figure 1** Topography and crater distributions of Helene. (a) Global topographic map of Helene with colors representing topographic height relative to the geometric center. (b) Regional map with heavily cratered terrain (red), moderately cratered terrain (yellow), less cratered terrain (blue), features unidentified (gray), and no images obtained (white). Black circles indicate large craters (~10 km). (c) Relative size-frequency distribution of craters of heavily cratered terrain (H), moderately cratered terrain (M), and less cratered terrain (L) of Helene as well as Telesto, Tethys, and Dione. The data for Tethys and Dione come from Kirchoff and Schenk [2010]. Colors represent regions in Figure 1b.

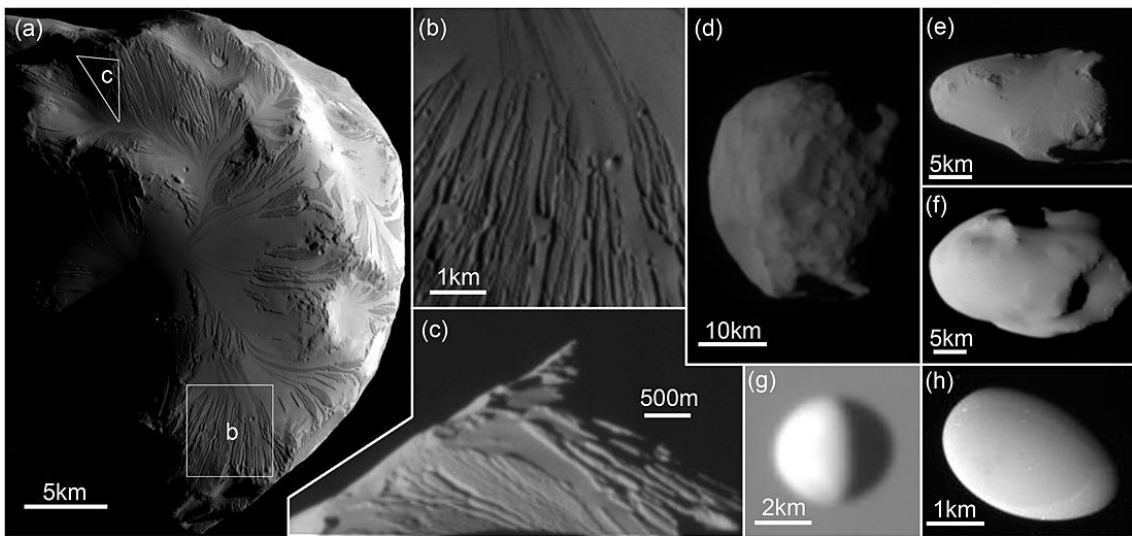


**Figure 2** Small satellites in the E-ring region. (a) Helene's leading hemisphere (image N1687119539). Insets indicate locations of Figures 2b and 2c. (b) Close-up image of the streaky depressions (N1687119539; 42 m/pixel). (c) The highest-resolution image of Helene (N1646317865; 24 m/pixel). The depths of the streaky features are estimated to be a few tens of meters. (d) Helene's trailing hemisphere (N1563643679). (e) Calypso's leading hemisphere (N1644754662). (f) Telesto's leading hemisphere (N1630076968). (g) Anti-Saturn side of Pallene with Saturn as a background (N1665947247; 223 m/pixel). (h) Methone's leading hemisphere (N00189072).

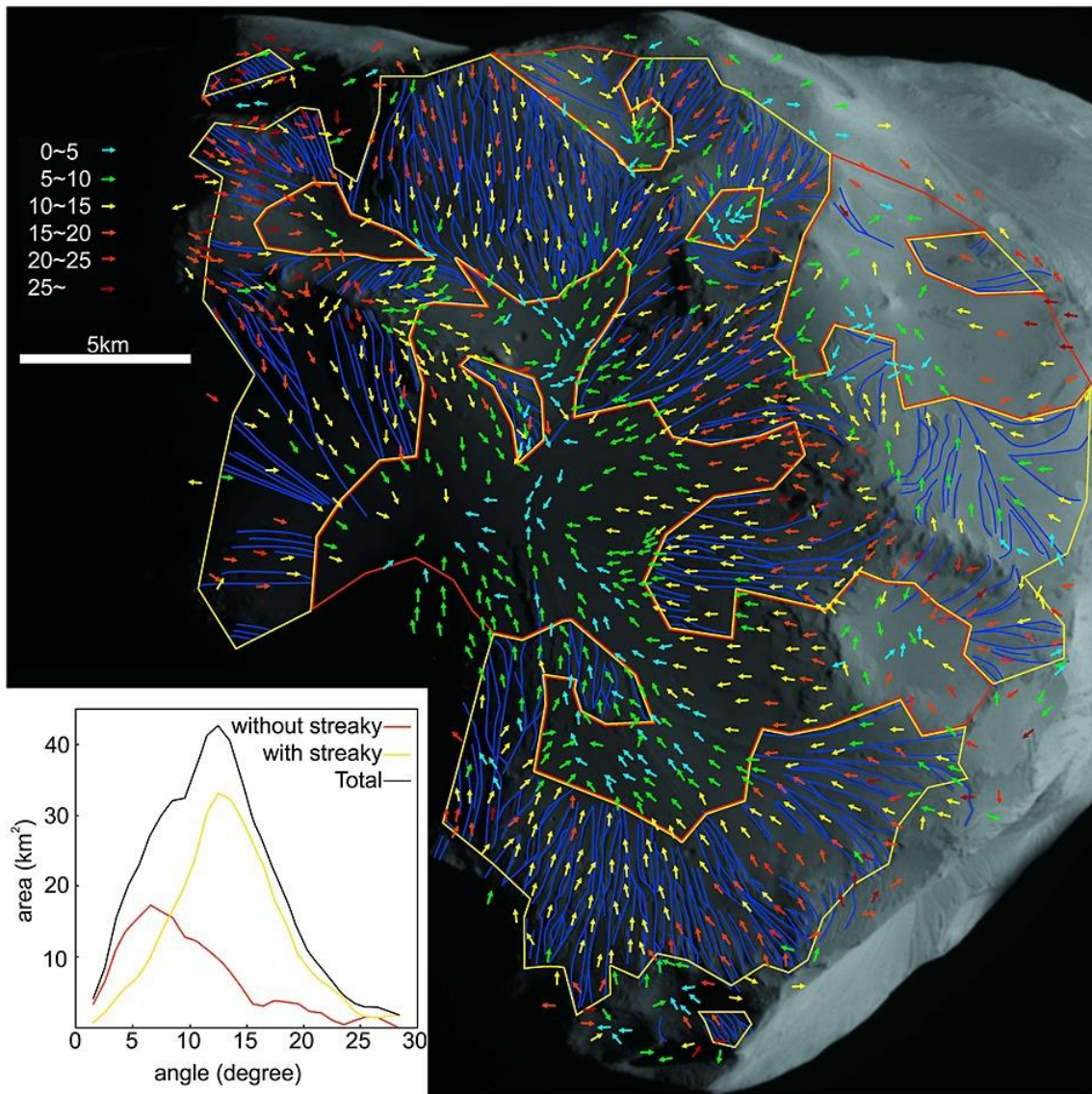


**Figure 3** The leading hemisphere of Helene (N1687120437) with arrows (located at the centers of triangles of the shape-model) indicating the directions of the local gravity (color represents slopes). Blue lines indicate streaky depressions. The regions enclosed by yellow or red lines are the regions with and without streaky depressions, respectively. Streaky features exist on steeper ( $> \sim 7$  degree) and strictly follow the directions of surface gravity. Inset shows the total areas of both regions as a function of slope angle (see Table S3 in supporting information). The horizontal axis is a moving average of  $\pm 1.5$  degree for the total area of the angle  $\pm 0.5$  degree.

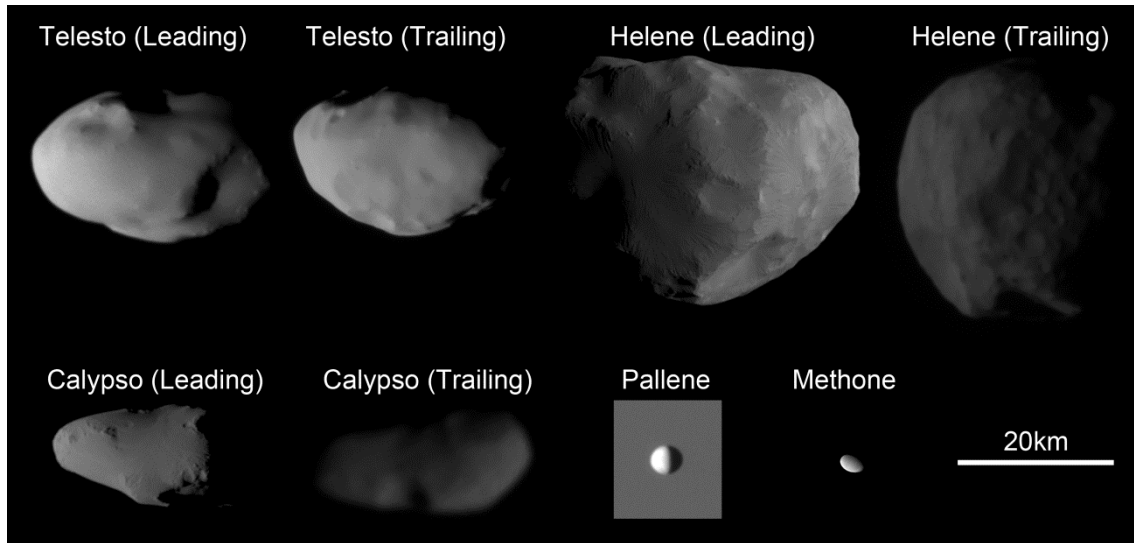


**Figure S1.** Small satellites in the E-ring region shown in the same scale (Cassini images N168712110 and N1563643679 for Helene; N1630076968 and N1514163666 for Telesto; N1644754662 and N1506184171 for Calypso; N1665947247 for Pallene; and N00189072 for Methone). Leading and Trailing indicate the leading and trailing hemispheres, respectively.

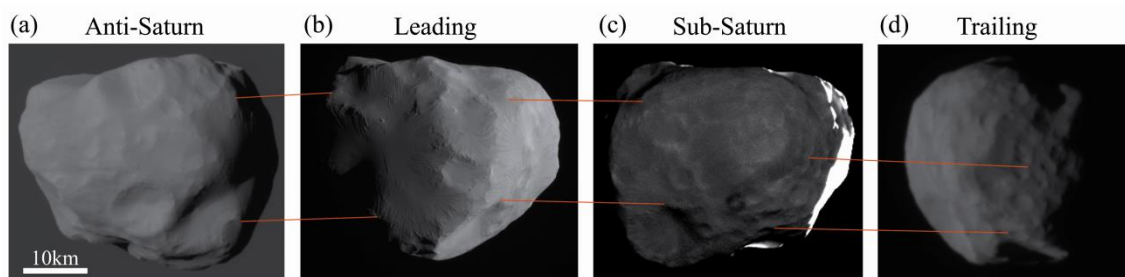


**Figure S2.** Images used for constructing the shape model (not all of them; see Table S1). Red lines connect the same signature points between images. (Image numbers from left to right, N1646319549, N1687121104, N1646315085, and N1563643679).

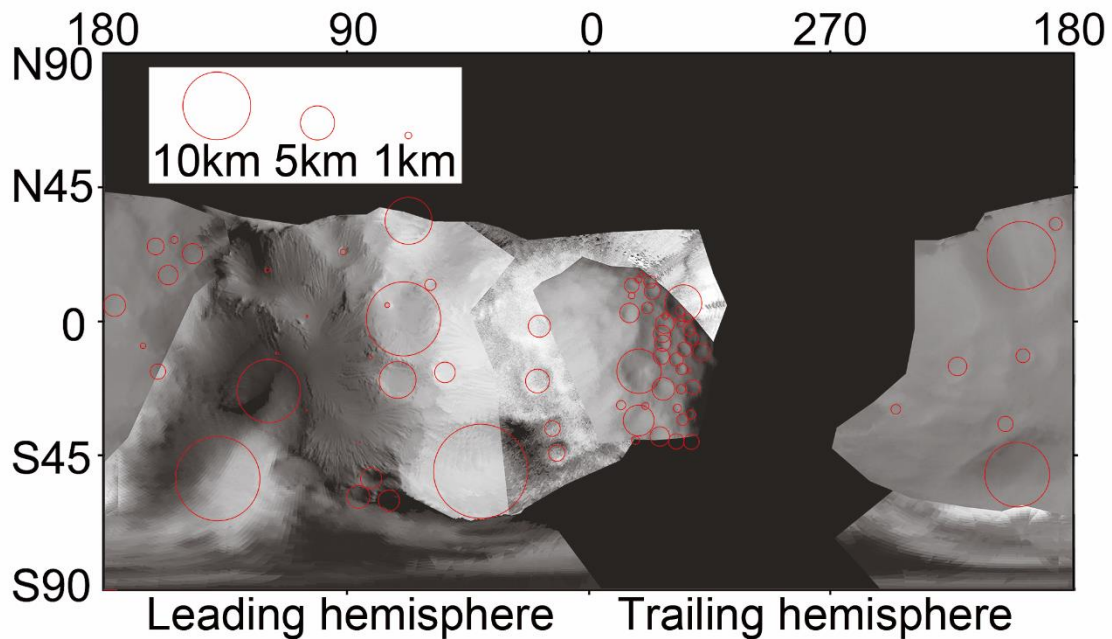


**Figure S3.** The distribution of craters (red circles) on Helene on a cylindrically-projected global image created from images listed in Table S1. Black region lacks images (craters cannot be identified in this region). Note that we identified craters in raw images rather than this projected image. Some craters on the anti-Saturn side of the trailing hemisphere (longitude 180-270) might remain unidentified due to low solar incidence angles of the images.

#### References

- Buratti, B. J., J. A. Mosher, and T. V. Johnson (1990), Albedo and color maps of the Saturnian satellites, *Icarus*, 87(2), 339– 357.
- Buratti, B. J., J. M. Bauer, M. D. Hicks, J. A. Mosher, G. Filacchione, T. Momary, K. H. Baines, R. H. Brown, R. N. Clark, and P. D. Nicholson (2010), Cassini spectra and photometry 0.25-5.1  $\mu$  m of the small inner satellites of Saturn, *Icarus*, 206(2), 524– 536.
- Filacchione, G., et al. (2010), Saturn's icy satellites investigated by Cassini–VIMS: II. Results at the end of nominal mission, *Icarus*, 206(2), 507– 523.
- Filacchione, G., et al. (2013), The radial distribution of water Ice and chromophores across Saturn's system, *Astrophys. J.*, 766(2).
- Howett, C. J. A., J. R. Spencer, J. Pearl, and M. Segura (2010), Thermal inertia and bolometric Bond albedo values for Mimas, Enceladus, Tethys, Dione, Rhea and Iapetus as derived from Cassini/CIRS measurements, *Icarus*, 206(2), 573–593

- Jaumann, R., R. N. Clark, F. Nimmo, A. R. Hendrix, B. J. Buratti, T. Denk, J. M. Moore, P. M. Schenk, S. J. Ostro, and R. Srama (2009), Icy satellites: Geological evolution and surface processes, in *Saturn from Cassini-Huygens*, edited by M. K. Dougherty et al., pp. 637– 681, Springer, New York.
- Kargel, J. S. (2006), Perspective - Enceladus: Cosmic gymnast, volatile miniworld, *Science*, 311(5766), 1389– 1391, doi:10.1126/science.1124495.
- Kirchoff, M. R., and P. Schenk (2009), Crater modification and geologic activity in Enceladus' heavily cratered plains: Evidence from the impact crater distribution, *Icarus*, 202(2), 656– 668.
- Kirchoff, M. R., and P. Schenk (2010), Impact cratering records of the mid-sized, icy saturnian satellites, *Icarus*, 206(2), 485– 497.
- Lambe, T. W., and R. V. Whitman (1979), *Soil Mechanics*, SI version, Wiley, New York.
- McClung, D., and P. A. Schaerer (1993), *The Avalanche Handbook*, Mountaineers, Seattle, Wash.
- Meyer, J., and J. Wisdom (2007), Tidal heating in Enceladus, *Icarus*, 188(2), 535– 539.
- Ostro, S. J., et al. (2010), New Cassini RADAR results for Saturn's icy satellites, *Icarus*, 206(2), 498– 506
- Pitman, K. M., B. J. Buratti, and J. A. Mosher (2010), Disk-integrated bolometric Bond albedos and rotational light curves of saturnian satellites from Cassini Visual and Infrared Mapping Spectrometer, *Icarus*, 206(2), 537– 560.
- Roberts, J. H., and F. Nimmo (2008), Tidal heating and the long-term stability of a subsurface ocean on Enceladus, *Icarus*, 194(2), 675– 689.
- Schenk, P., D. P. Hamilton, R. E. Johnson, W. B. McKinnon, C. Paranicas, J. Schmidt, and M. R. Showalter (2011), Plasma, plumes and rings: Saturn system dynamics as recorded in global color patterns on its midsize icy satellites, *Icarus*, 211(1), 740– 757.
- Showman, A. P., L. Han, and W. B. Hubbard (2013), The effect of an asymmetric core on convection in Enceladus' ice shell: implications for south polar tectonics and heat flux, *Geophys. Res. Lett.*, 40, 1– 5.
- Thomas, P. C., J. A. Burns, M. S. Tiscareno, M. M. Hedman, and P. Helfenstein (2013), Saturn's mysterious arc-embedded moons: Recycled fluff?, abstract presented at 44th Lunar and Planetary Science Conference, Lunar and Planetary Institute and Universities Space Research Association, Houston, Tex.
- Verbiscer, A. J., and J. Veverka (1992), Mimas - Photometric roughness and albedo map, *Icarus*, 99(1), 63– 69.
- Verbiscer, A., R. French, M. Showalter, and P. Helfenstein (2007), Enceladus: Cosmic

graffiti artist caught in the act, *Science*, 315(5813), 815.

Zahnle, K., P. Schenk, H. Levison, and L. Dones (2003), Cratering rates in the outer Solar System, *Icarus*, 163(2), 263– 289.

## **Supplementary Information**

### **Crater on Helene**

As observed on most satellites of Saturn, Helene has numerous craters. Using the high-resolution images, we identify more than 70 craters. Craters are identified by (i) a circular depression with a rim, (ii) a depression imaged with a resolution of at least 5 pixels for clear understanding of its shape, and (iii) a depression identified in more than one image. Larger craters (> 10 km) on north and south polar terrain are also verified by our shape model. Craters are not uniformly distributed over the surface of Helene (Fig. S3). At least 5 craters are larger than ~10 km in diameter and at least 8 craters are 5 to 10 km in diameter. They are almost uniformly distributed over the entire surface of Helene. In contrast, the number of small craters (below 5 km in diameter) varies significantly depending on the region. We identify three distinct regions based on the crater densities, such as (i) heavily cratered terrain (red in Fig. 1b), which covers the sub-Saturn side of the trailing hemisphere (we identify 38 craters ranging from 0.7 km to 10 km in diameter), (ii) moderately cratered terrain (yellow in Fig. 1b), which covers the anti-Saturn side of the trailing hemisphere (14 craters ranging from 0.2 km to 12 km), and (iii) less cratered terrain (blue in Fig. 1b), which covers the leading hemisphere (22 craters ranging from 1 km to 10 km). We note that crater identifications in the moderately cratered terrain suffered from low solar-incidence angles in most images of this region. The locations and distributions of identified craters are shown in Fig. S3. Fig. 1c shows crater size-frequency distributions in a relative plot (R-plot; the ratio of the differential form of cumulative crater-size distribution to a size-frequency distribution with differential slope equal to 3. Error bars are defined as  $\pm R \cdot N^{-0.5}$ , where N is the number of craters between a bin. Similarly, we analyze the Telesto's trailing hemisphere to obtain the R-plot, which is shown in Fig. 1c. For these analyses, we follow the method of Crater Analysis Technique Working Group [1979].

### **Numerical shape model**

To develop a numerical shape model, we follow the previously

proposed method [Hartley and Zisserman, 2003] by using 16 high-resolution images shown in Table S1 to develop a shape model. We i) split the surface of Helene into 10 parts; ii) select 3 images from the 16 high-resolution images showing a particular part of the body; iii) identify at least 8 corresponding points in all of these 3 images; and iv) measure both relative locations of these corresponding points and camera positions of 3 images using the epipolar geometry, which results in forming a local shape model (Fig. S2). We perform the process of ii) to iv) for all 10 parts of Helene before binding the local shape models into a single very-rough shape model (Table S2).

Once a shape model is developed, a camera position for each image can be precisely determined. We then perform stereo analyses for all of the 16 high-resolution images with the camera positions determined to obtain the exact locations of 750 control points, which results in quality improvement of the shape model. We compare the shape model to all of the high-resolution images obtained by the Cassini spacecraft to confirm that the shape model properly reproduces outlines and features in these images. In particular, the leading hemisphere is carefully analyzed by defining 1024 polygons to critically compare the local gravity and the directions of streaky depressions.

We develop a topographic map of Helene based on the shape model assuming that the center of mass coincides with the geometric center (Fig. 1a). The map enables us to identify the existence of basins, which are divided by ridges. We assume a constant density throughout the body, which might not be realistic for deriving the exact values of gravity but is adequate for obtaining approximate gravity-vector orientations and determination of downslope directions.

We constructed the numerical shape model as the assemblage of 7492 small tetrahedrons, whose densities were assumed to be the same. The leading hemisphere is specifically analyzed carefully by defining 1024 polygons. To derive the local gravity, we i) measure the distance between the geometric center of a single tetrahedron at the centroid of a given polygon; ii) calculate the gravitational vector from the distance and the volume of the tetrahedron; iii) perform i) and ii) for all tetrahedrons consisting of the shape model; iv) integrate these gravitational vectors obtained by iii) to obtain the total gravity acceleration from entire Helene at the given polygon; v) calculate the inner product between the normal vector of the polygon and the total gravitational vector on the polygon to obtain the angle of the slope; vi) remove

the component along the normal vector of the polygon from the gravitational vector to obtain the direction of the local gravity on the polygon; vii) perform i) to vi) for all 1024 polygons consisting of the surface of leading hemisphere.

### **Lack of hemispheric dichotomy for Telesto/Calypso**

We consider that the lack of hemispheric dichotomy for Telesto/Calypso can be explained by either non-synchronous rotation or the motion of the E-ring particles. The latter case is discussed below.

The dynamics of the E-ring particles are difficult to directly observe and can be surprisingly complex due to the competing effects of the gravity of satellites, solar radiation pressure, electrostatic grain potential, the Lorenz forces, the plasma-sputtering, and plasma drag [Horányi *et al.*, 2008, 2009]. Nevertheless, these forces cause large orbital eccentricities or an increasing of semi-major axes, which result in correspondingly large radial excursions of E-ring particles in just a few years [Horányi *et al.*, 1992, 2009]. Especially, large orbital eccentricities of E-ring particles having the semi-major axis close to Enceladus can play an important role in the hemispheric dichotomies on satellites. Within the orbit of Enceladus, E-ring particles move faster than satellites, which causes E-ring particles to collide preferentially onto the trailing side of Mimas. On the other hand, beyond the orbit of Enceladus, E-ring particles move slower and are overtaken by satellites, which causes E-ring particles to collide preferentially onto the leading side of Dione and Tethys. This can also explain Helene's hemispheric dichotomy.

Unlike Helene, Telesto and Calypso only faintly show a hemispheric dichotomy (e.g., Telesto's leading hemisphere has a relatively smoother and relatively less cratered surface than the trailing side). This, again, could be explained by the differences between the relative velocities of E-ring particles relative to Dione and Tethys. Because Tethys is closer to Enceladus than Dione, the velocities of E-ring particles in the orbit of Tethys is less decelerated compared with those in the orbit of Dione. Therefore, interactions with particles might not be concentrated significantly on the leading hemisphere of Tethys, Telesto, and Calypso.

### **Deposition of ring particles on Pallene and Methone**

Spherical shapes and smooth appearances of both Pallene and Methone might also be related to the dense E-ring particles at their orbits but might be complicated by the existence of the co-orbital ring and the arc coexisting with both Pallene and Methone (perhaps also Anthe, the other of



the Alkyonides), whose materials might originate from these satellites [Hedman *et al.*, 2009]. In any case, both of these tiny satellites are difficult to immediately accumulate materials released by impacts, which may temporarily form the ring or arcs. Nevertheless, these released materials, originally from both the E-ring and satellites, should re-accumulate on the satellites because of the confinement of dust in resonances with Mimas or Enceladus [Hedman *et al.*, 2009]. These processes may explain their unusual smooth surfaces and spherical shapes. We suspect that Anthe also has a spherical shape with a smooth appearance.

### **Age estimates based on cratering rate**

Because of the nature of crater chronology, the crater densities on Enceladus do not directly indicate when Enceladus' cryovolcanism has begun (the crater densities on Enceladus may show a state of dynamic equilibrium between the cratering and resurfacing rates). The situation on Helene is different from that of Enceladus; particles from Enceladus may deposit over the surface of Helene but its thickness should be fairly thin (a few ten or hundred meters), while the depth of a crater is relatively deep enough (a crater with a few hundred meters diameter should have a few tens of meters depth). In other words, the E-ring depositions are difficult to bury newly-formed craters (larger than  $\sim 1$  km in diameter) after an initiation of the deposition. Thus, we consider that the deposits on Helene are suitable to discuss when the Enceladus' cryovolcanism has begun.

On Helene's E-ring deposit, whose area is  $1,637 \text{ km}^2$ , we identify 5 craters of  $\sim 200$  m in diameter but not exceeding 1 km. This clearly indicates young formational ages of the deposits, but estimating the ages can be more complicated than the cases on the Moon. This is mostly due to the lack of dated samples from the saturnian satellites and to the difficulty in determining the cratering rate, which should be estimated theoretically based on the populations and orbits of potential impactors. According to Dones *et al.* [2009], potential impactors come from (i) main-belt asteroids, (ii) trojan objects of the gas giants, (iii) Centaurs and ecliptic comets, (iv) Saturn's irregular satellites, (v) planetocentric bodies, and (vi) Nearly Isotropic Comets.

Previous theoretical studies for estimating formational ages of geological features on saturnian satellites [e.g. Zahnle *et al.*, 2003] are based either on (A) the crater densities on the Moon, Europa, Ganymede, and Triton, and (B) the statistics of encounter with potential impactors, such as comets

and asteroids. Trans-Saturnian objects, such as Centaurs, are considered as the major impactors. Their populations and orbital properties [*Gladman et al.*, 2001] are studied with ground-based observations, even though the accurate size-frequency of small objects is still unknown because of their great distances. *Zahnle et al.* [2003] estimates the cratering rate for the outer solar system, including that on saturnian small satellites; for example, the cratering rate for objects larger than 1 km in diameter on Helene is (A)  $2.0 \times 10^{-7}$  craters per  $10^3 \text{ km}^2$  per year if we assume that small objects obey a nearly collisional distribution and (B)  $2.0 \times 10^{-9}$  craters per  $10^3 \text{ km}^2$  per year if we assume the size–number distribution is like that inferred at Jupiter. Therefore, assuming this cratering rate, the formational ages of the E-ring deposits on Helene are likely to be 0.3-5 My (the former case) or 200-500 My (the latter case).

On the other hand, according to *Dones et al.* [2009] if major potential impactors originated from heliocentric objects, such as Centaurs, impact cratering on saturnian satellites should exhibit a hemispheric dichotomy because heliocentric impactors strongly favor cratering of the leading hemisphere. However, small craters on saturnian satellites do not show such dichotomies, which may imply that planetocentric impactors, such as secondary impactors, are dominant to form smaller craters. If we assume that the heavily cratered regions on Helene, which have 100 craters larger than 1 km in diameter per  $1000 \text{ km}^2$ , was formed more than 4 Gy and that the cratering rate is constant for its life time, we obtain  $\sim 40$  My for the formational age of the E-ring deposit on Helene. Or, if we assume the crater distributions of Dione [*Kirchoff and Schenk*, 2010], whose Trojan satellites include Helene, indicate that the crater formation rates of  $> 1 \text{ km}$  craters is  $7.5 \times 10^{-6}$  craters per  $10^3 \text{ km}^2$  per year and of  $> 200 \text{ m}$  craters is  $\sim 10^{-7}$  craters per  $10^3 \text{ km}^2$  per year, we obtain  $\sim 50$  My for the formational age of the E-ring deposit on Helene.

We note that these estimates include ambiguities in their assumptions. However, importantly, all these independent estimates coincide around several 10 My. Thus, we conclude several tens of million years or younger for the most likely formational ages of E-ring deposit on Helene.

## References

Crater Analysis Techniques Working Group (1979), Standard Techniques for Presentation and Analysis of Crater Size-Frequency Data, *Icarus*, 37,

- Dones, L., C. R. Chapman, W. B. McKinnon, H. J. Melosh, M. R. Kirchoff, G. Neukum, and K. J. Zahnle (2009), Icy Satellites of Saturn: Impact Cratering and Age Determination, in *Saturn from Cassini-Huygens*, edited by M. K. Dougherty et al., pp. 613-635, Springer, NewYork.
- Gladman, B., J. J. Kavelaars, J. M. Petit, A. Morbidelli, M. J. Holman, and T. Loredó (2001), The structure of the Kuiper Belt: Size distribution and radial extent, *The Astronomical Journal*, *122*(2), 1051-1066, doi:10.1086/322080.
- Hartley, R., and A. Zisserman (2003), *Multiple view geometry in computer vision. 2nd edition*, Cambridge University Press, Cambridge, UK.
- Hedman, M. M., C. D. Murray, N. J. Cooper, M. S. Tiscareno, K. Beurle, M. W. Evans, and J. A. Burns (2009), Three tenuous rings/arcs for three tiny moons, *Icarus*, *199*(2), 378-386, doi:10.1016/j.icarus.2008.11.001.
- Horányi, M., A. Juhász, and G. E. Morfill (2008), Large-scale structure of Saturn's E-ring, *Geophysical Research Letters*, *35*(4), L04203, doi:10.1029/2007GL032726.
- Horányi, M., J. A. Burns, M. M. Hedman, G. H. Jones, and S. Kempf (2009), Diffuse Rings, in *Saturn from Cassini-Huygens*, edited by M. K. Dougherty et al., pp. 511-536, Springer, NewYork.
- Horanyi, M., J. A. Burns, and D. P. Hamilton (1992), The Dynamics of Saturns E Ring Particles, *Icarus*, *97*(2), 248-259.
- Kirchoff, M. R., and P. Schenk (2010), Impact cratering records of the mid-sized, icy saturnian satellites, *Icarus*, *206*(2), 485-497, doi:10.1016/j.icarus.2009.12.007.
- Zahnle, K., P. Schenk, H. Levison, and L. Dones (2003), Cratering rates in the outer Solar System, *Icarus*, *163*(2), 263-289, doi:10.1016/S0019-1035(03)00048-4.

**Table S1. Images used for analyses of a shape model of Helene.**

Image	Date (UTC)	Range (km)	Resolution (m/pixel)	Sub-Cassini		Sub-Solar	
				Lat.	Lon.	Lat.	Lon.
N1519536732	2006-2-25	67836	423.7	-0.4	96.6	-18.5	187.2
N1519537272	2006-2-25	68271	426.4	-0.4	93.6	-18.5	188.0
N1534480072	2006-8-27	50353	314.5	73.8	31.0	-16.2	237.9
N1534483492	2006-8-27	61949	387.0	75.4	138.9	-16.2	243.0
N1563643679	2007-7-20	38890	242.9	-2.5	316.2	-11.4	13.4
N1563644326	2007-7-20	38466	240.3	-2.6	321.6	-11.4	14.4
N1506207298	2008-11-24	69067	431.4	25.7	347.3	-3.9	329.6
N1646315085	2010-3-3	22073	137.9	-3.8	4.0	3.2	193.1
N1646319549	2010-3-3	18821	117.6	-3.6	183.0	3.2	199.9
N1646320608	2010-3-3	28482	177.9	-2.2	186.0	3.2	201.5
W1646317554	2010-3-3	1911	119.4	-42.4	116.4	3.2	196.9
W1646317899	2010-3-3	4113	256.9	-18.2	164.8	3.2	197.1
N1675165048	2011-1-31	31434	190.3	-3.5	114.3	8.2	173.3
N1687119135	2011-6-18	7355	44.5	2.7	147.3	10.1	19.2
N1687121104	2011-6-18	9800	59.3	1.3	87.4	10.1	22.2
N1687121464	2011-6-18	11031	66.8	1.0	81.8	10.1	22.8

**Table S2. The distance (in meter) between the geometric center and the surface based on the shape model of Helene (latitudes in horizontal lines and longitudes in vertical lines)**

	-90	-80	-70	-60	-50	-40	-30	-20	-10	0
10	15719	16069	17066	17412	17580	17316	17762	18518	18627	19301
20	15719	16118	17164	17965	17136	16887	16965	17477	17615	19290
30	15719	16788	17667	17833	16614	15878	16488	17165	17942	19555
40	15719	16832	18213	17387	16331	15584	16611	17680	18183	19842
50	15719	17436	18514	18063	16891	16483	17713	19066	19259	20455
60	15719	17083	18489	18551	17935	17599	19735	20206	21084	21303
70	15719	16629	18600	19465	18868	19917	21033	21439	21834	21483
80	15719	16860	18305	19950	20168	20823	20662	20580	21029	21519
90	15719	16642	18014	19834	20371	19991	19891	19973	20445	20190
100	15719	17323	17578	19500	20204	19788	19120	19000	19083	19171
110	15719	16775	17773	18689	19949	19526	18859	18368	18413	18304
120	15719	16493	17154	18547	19206	19136	18405	17958	17485	17800
130	15719	16950	17247	19127	18399	18584	17652	17296	17209	17786
140	15719	16684	17029	18054	17497	16505	16472	17584	17829	18238
150	15719	16422	17193	17202	15845	15814	16503	17854	18791	18907
160	15719	16620	17375	16870	15976	16579	17272	18618	19780	19309
170	15719	16422	16842	17088	16409	17156	18150	19477	19448	19366
180	15719	16471	16842	16941	17107	17454	17799	18700	18445	18991
190	15719	16169	16379	16599	15755	15712	16400	17789	18065	18734
200	15719	15829	16120	16469	15041	14804	16174	17994	18074	18438
210	15719	15892	15939	16302	14986	14933	16598	17877	18345	19109
220	15719	15463	15705	16039	15444	16170	16367	17738	17904	19962
230	15719	15426	15421	15729	15655	15901	16347	17168	18645	19985
240	15719	15245	15316	15385	15476	15630	16243	18403	19761	20758
250	15719	15033	15019	15713	15213	15810	17398	19787	20155	19799
260	15719	14827	15143	15834	15317	15910	17476	18864	19565	19366
270	15719	14721	14828	15979	15638	15834	16764	18138	19620	19654
280	15719	14721	14764	16167	16272	16289	17253	17600	19152	20311
290	15719	15081	14699	16137	17002	17549	18013	18626	19235	20560
300	15719	14751	15010	15727	17884	18929	18927	19303	19840	20999
310	15719	14631	14698	15496	16788	19341	21007	20913	21313	23335
320	15719	14689	14624	15242	16385	19013	21797	23464	22170	23716
330	15719	14990	15116	15254	16356	18645	21024	22527	22825	24493
340	15719	15095	15299	16394	17989	18658	20591	22377	23696	24295
350	15719	15495	16033	17199	18424	18873	19090	20513	22235	23889
360	15719	15448	16041	17513	18104	17938	18441	19771	20585	21219

**Table S2. Continued**

	<b>10</b>	<b>20</b>	<b>30</b>	<b>40</b>	<b>50</b>	<b>60</b>	<b>70</b>	<b>80</b>	<b>90</b>
<b>10</b>	21110	21699	20990	21250	17418	15180	14501	14501	14123
<b>20</b>	19741	20372	21452	20763	18191	14735	14735	14287	14123
<b>30</b>	19724	20289	21407	20435	17267	15683	14287	13796	14123
<b>40</b>	20360	20946	20984	20420	18149	15075	15075	13796	14123
<b>50</b>	20839	21721	21270	19618	17323	15790	14996	14996	14123
<b>60</b>	21115	20943	19210	18956	17693	16577	14996	14415	14123
<b>70</b>	21676	21636	19871	18491	18358	15799	15257	14415	14123
<b>80</b>	21169	20968	20128	18906	18127	16118	15257	14874	14123
<b>90</b>	20488	20593	20619	19961	18550	17017	14874	14874	14123
<b>100</b>	19355	19766	19965	19896	18960	17602	15093	14395	14123
<b>110</b>	18664	18971	19565	19568	18650	16792	15093	14395	14123
<b>120</b>	18336	18792	19290	19966	18449	16860	15425	15425	14123
<b>130</b>	18842	18882	19463	19914	18576	17229	14680	14680	14123
<b>140</b>	18975	19689	19493	19744	18066	16745	15382	14680	14123
<b>150</b>	19892	20587	20282	19704	18495	15688	15688	14085	14123
<b>160</b>	19437	20404	20255	20236	18057	15872	14906	14085	14123
<b>170</b>	19885	19626	19090	19412	18021	16207	14906	14085	14123
<b>180</b>	18384	18796	18067	18318	17847	15978	15370	14443	14123
<b>190</b>	18416	18646	19504	19225	17566	15339	14443	14443	14123
<b>200</b>	18809	18173	18182	18656	17500	15912	14443	14443	14123
<b>210</b>	20217	18599	18611	18428	16851	15108	15108	13802	14123
<b>220</b>	19348	18668	19876	17972	16686	15618	14365	13802	14123
<b>230</b>	18947	18183	19082	17919	16843	15618	14365	13802	14123
<b>240</b>	18796	18120	17904	17510	16841	14891	14891	13802	14123
<b>250</b>	19151	18110	18039	18296	15774	15774	14141	14141	14123
<b>260</b>	19405	18434	19003	18438	16835	14970	14141	14141	14123
<b>270</b>	20183	19375	20207	19341	16546	14970	14970	14141	14123
<b>280</b>	21280	21238	21525	20015	16663	15683	14633	13796	14123
<b>290</b>	21432	21322	21044	19289	17001	14633	14633	13796	14123
<b>300</b>	22323	21829	21497	18880	16428	15365	13796	13796	14123
<b>310</b>	24042	23414	21414	18364	16768	15365	14376	13796	14123
<b>320</b>	24860	24022	23296	19191	15850	14376	14376	14376	14123
<b>330</b>	25153	26533	24608	19913	17419	15850	14376	13888	14123
<b>340</b>	25363	25322	24404	20236	16073	14820	13888	13888	14123
<b>350</b>	23330	22643	21239	21370	17362	14820	13888	13888	14123
<b>360</b>	22822	21701	20832	20573	18902	15577	14501	13888	14123

**Table S3. Angles of slopes to areas calculated from the shape model of Helene.**

Angle	Area with streaky depressions (km <sup>2</sup> )	Area without streaky depressions (km <sup>2</sup> )	Total (km <sup>2</sup> )
0 ~ 1	0.00	2.23	2.23
1 ~ 2	0.70	2.88	3.58
2 ~ 3	1.54	4.81	6.35
3 ~ 4	3.86	11.62	15.48
4 ~ 5	7.04	16.75	23.79
5 ~ 6	6.65	13.18	19.83
6 ~ 7	8.48	16.88	25.36
7 ~ 8	14.75	21.54	36.30
8 ~ 9	17.52	10.81	28.33
9 ~ 10	17.58	14.17	31.75
10 ~ 11	23.97	13.37	37.34
11 ~ 12	31.08	9.52	40.60
12 ~ 13	35.80	10.27	46.08
13 ~ 14	32.15	9.22	41.36
14 ~ 15	29.45	4.93	34.38
15 ~ 16	27.17	2.86	30.04
16 ~ 17	21.58	2.34	23.92
17 ~ 18	19.83	3.88	23.72
18 ~ 19	12.43	5.35	17.78
19 ~ 20	11.34	1.18	12.53
20 ~ 21	7.18	3.59	10.78
21 ~ 22	6.09	1.96	8.05
22 ~ 23	6.36	0.57	6.93
23 ~ 24	3.87	0.49	4.36
24 ~ 25	2.31	0.00	2.31
25 ~ 26	0.55	2.67	3.22
26 ~ 27	1.44	1.83	3.27
27 ~ 28	2.05	0.00	2.05
28 ~ 29	1.63	0.00	1.63
> 29	1.07	0.00	1.07